

See discussions, stats, and author profiles for this publication at: <https://www.researchgate.net/publication/263956351>

# Active Control of Evaporative Solution Deposition by Modulated Infrared Illumination

ARTICLE in THE JOURNAL OF PHYSICAL CHEMISTRY C · MAY 2012

Impact Factor: 4.77 · DOI: 10.1021/jp301092y

---

CITATIONS

2

---

READS

19

## 4 AUTHORS, INCLUDING:



[Jorge Vieyra](#)

Technische Universiteit Eindhoven

7 PUBLICATIONS 7 CITATIONS

SEE PROFILE



[Jasper J Michels](#)

Max Planck Institute for Polymer Research

43 PUBLICATIONS 999 CITATIONS

SEE PROFILE



[Anton A. Darhuber](#)

Technische Universiteit Eindhoven

114 PUBLICATIONS 2,016 CITATIONS

SEE PROFILE

# Active Control of Evaporative Solution Deposition by Modulated Infrared Illumination

Jorge A. Vieyra Salas,<sup>†,‡</sup> Jørgen M. van der Veen,<sup>†</sup> Jasper J. Michels,<sup>§</sup> and Anton A. Darhuber<sup>\*,†</sup>

<sup>†</sup>Mesosopic Transport Phenomena Group, Department of Applied Physics, Eindhoven University of Technology, P.O. Box 513, 5600MB Eindhoven, The Netherlands

<sup>‡</sup>Dutch Polymer Institute (DPI), P.O. Box 902, 5600AX Eindhoven, The Netherlands

<sup>§</sup>Holst Centre/TNO, High Tech Campus 31, 5656AE Eindhoven, The Netherlands

## S Supporting Information

**ABSTRACT:** We designed and built a highly adaptive and flexible system based on modulated infrared irradiation for the active control of evaporative material deposition suitable for solution processing of organic electronic materials. We performed systematic experiments using thick layers of a high molecular weight aqueous dispersion of poly(3,4-ethylene-dioxythiophene):poly(styrenesulfonate) (PEDOT:PSS) nanoparticles as well as thin layers of light-emitting polymers in an organic solvent. We identified two complementary deposition modes, where material accumulates either in the illuminated or the nonirradiated regions, depending on the molecular weight of the solute and the solution layer thickness. We developed numerical models that account for heat transfer due to infrared illumination, solvent evaporation into the gas phase, and solute redistribution in the liquid layer. The computational results agree well with the experimental observations regarding the solute depletion and accumulation behavior.



## I. INTRODUCTION

Solution deposition processes such as inkjet-printing and spray-, dip-, die-, or spin-coating are promising techniques for low-cost manufacture of organic electronic devices.<sup>1–31</sup> Materials are dissolved in suitable solvents and subsequently deposited on a substrate, which leaves a dry layer upon evaporation of the solvent. While inkjet printing intrinsically provides the possibility for pattern generation, dip- and die-coating are usually preferred when layer thickness uniformity, high processing speeds, and large-area compatibility are desired. A combination of such a coating method with a noninvasive technique for pattern generation could potentially provide a high flexibility for roll-to-roll fabrication of organic electronic devices.

A number of groups have investigated the light-induced pattern formation in polymer solutions and suspensions of colloidal particles. Hofkens et al. observed pattern formation in polymer solutions irradiated with a near-infrared laser, which they ascribed to radiation pressure exerted by the focused laser beam.<sup>32</sup> Sigel et al. reported a nonphotothermal material organization induced by continuous-wave visible laser light at low power levels in entangled solutions of polymers of sufficiently high molecular mass and optical anisotropy along the chain backbone.<sup>33</sup> Dietzel and Poulikakos presented numerical simulations of the response of droplets containing highly absorbing nanoparticles to irradiation with axisymmetric laser beams.<sup>34</sup> Kossyrev et al. used ultraviolet holographic lithography to create periodic cross-links and density variations of photopolymerizable monomers and polymers dissolved in a volatile solvent and their influence on the dry layer morphology.<sup>35</sup> Nabetani et al. studied the laser-induced

formation and deposition of polymer assemblies upon solvent evaporation using both single and multiple optical traps.<sup>36</sup> Performing similar experiments, Louchev et al. argued for the importance of Marangoni convection for the polymer mass transfer process.<sup>37</sup> Anyfantakis et al. observed the laser-light-induced formation of micrometer-sized filaments with a length up to several centimeters as well as filament arrays in polybutadiene solutions.<sup>38</sup> Delville et al. analyzed the morphology and properties of solid deposits from a photoactive solution induced by two interfering laser beams.<sup>39</sup>

While these illumination-based mechanisms are contactless and thus very flexible, they are not immediately convenient for a continuous fabrication process. Most of them require a tightly focused laser beam with high spatial intensity gradients, optical elements in close proximity to the solution layer, or a photoreactive material system. In order to maximize the independence from specific solute–solvent–substrate material combinations, we explore the use of spatially and temporally modulated infrared (IR) irradiation to control the solvent evaporation and solute deposition process. Instead of sequential point-by-point processes implied by focused laser beams, we utilize a digital multimirror device with 1024 × 768 independently controllable micromirrors that allow for maskless pattern formation in a parallel fashion with a high degree of flexibility.

Liquid thickness modulations due to IR-induced soluto- and thermocapillary flow have been applied for the visualization of

Received: February 2, 2012

Revised: April 26, 2012

Published: May 23, 2012



IR intensity distributions and IR photography before the advent of IR cameras.<sup>40–42</sup> Hitt and Smith calculated the effect of localized thermal radiation on the evolution of a liquid film subject to thermocapillary stresses.<sup>43</sup> Grigoriev<sup>44</sup> presented a theoretical and numerical model for controlling and suppressing evaporative instabilities of a thin liquid layer by means of modulated IR illumination. Garnier et al. irradiated an absorbing substrate with spatially modulated visible light to locally suppress a thermocapillary fingering instability.<sup>45</sup>

## II. EXPERIMENTAL METHODS

We designed and built an infrared illumination setup consisting of an IR laser in combination with a digital multimirror device (DMD, Texas Instruments, model 1076-746c). The DMD consists of  $1024 \times 768$  individually controllable mirrors,  $10.8 \times 10.8 \mu\text{m}^2$  in size with a pitch of  $13.68 \mu\text{m}$ , which can be switched with a frame rate up to 16.3 kHz. Thus, the system not only allows for rapid temporal modulation but also spatial modulation of the illumination intensity in a parallel, nonsequential fashion. A schematic and a photograph of the setup are provided in Figure 1. In the “on” state the DMD

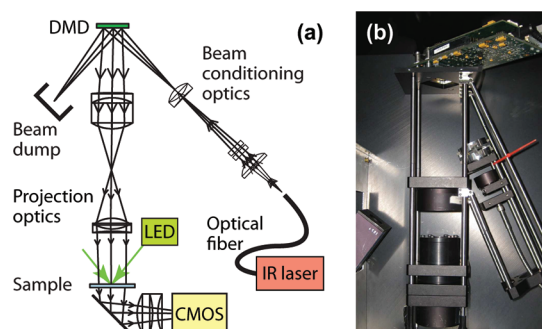


**Figure 1.** (a) Sketch and (b) photograph of the experimental setup. Image height 35 cm.

mirrors reflect light incident under an angle of  $12^\circ$  relative to the optical axis in the direction normal to the front face of the DMD device. In the “off” state the light is directed into a beam-dump.

We used a fiber-coupled laserdiode (Lumics, model number LU1470C020-C) operating at a wavelength of  $\lambda = 1470 \text{ nm}$  with a maximum optical power output of 20 W. This wavelength was selected because of a local maximum of the optical absorption coefficient of water, the availability of high power laser sources, and a high transmission of the DMD protective front face window. The optical fiber has a core diameter of  $400 \mu\text{m}$  with a numerical aperture of 0.22. Subsequently, the light is collimated to a beam of 4.3 mm diameter. A custom-built beam homogenizing system, comprising two microlens arrays (Süss MicroOptics), was used to transform the Gaussian intensity distribution to a flat-top beam profile. A custom-designed double-telecentric lens system with a total magnification of  $1.75\times$  and diffraction limited performance with Airy disk diameter  $23.2 \mu\text{m}$  was used to project the image defined by the DMD mirrors onto the substrate. Due to the double telecentric lens design, the image plane is essentially perfectly flat with a nominal maximum defocus between the center and perimeter of  $0.62 \mu\text{m}$ . The low numerical aperture of 0.039 provides a large depth of field of approximately  $160 \mu\text{m}$ . The total power  $P_{100}$  incident on the sample, if all mirrors

were in the on state, could be varied between 0 and approximately 2.5 W.

For temperature control, a transparent heatsink was designed, comprising two 0.5 mm thick soda lime glass plates with a gap of 1 mm, through which cooling water from a thermostated bath (Julabo) was circulated. Samples were temporarily attached to the heatsink by means of a thin water layer. Below the cooling plate, an imaging system with a CMOS camera (Thorlabs) allows for online observation of the evaporation process. A Schott KG3 filter (not shown in Figure 1) prevented any IR radiation that was not absorbed by the cooling water from reaching the camera. For observation we used either a reflection mode, which is sensitive primarily to optical interference between the liquid–air and liquid–solid interfaces of the solution layer, or a transmission mode utilizing diffuse light from a green LED.

The IR projection setup was enclosed in an anodized metal box of approximate dimensions  $40 \times 25 \times 50 \text{ cm}^3$ , at the bottom of which the heatsink and the observation optics were attached. A filtered air flow with a rate between 0 and 20 L/min was maintained inside the enclosure and an exhaust connection with a slight negative pressure was attached.

We used two types of solutions for the experiments. The first was an aqueous dispersion of poly(3,4-ethylenedioxythiophene)–poly(styrenesulfonate) (PEDOT:PSS, Clevis AI4083, Heraeus). The second type of solution consisted of red and blue light-emitting polymers (LEPs, Merck KGaA) dissolved in mesitylene with initial concentrations of approximately 1 wt %. These materials are commonly used as hole transport layers and light emitters in organic light emitting diodes (OLEDs).

Samples were made from soda lime glass sheets with a thickness of either  $d_{\text{sl}} = 1 \text{ mm}$  or  $0.15 \text{ mm}$  that were cut to dimension of several centimeters. The  $0.15 \text{ mm}$  thin substrates were temporarily adhered to 1 mm thick slides of heat absorbing glass (KG3, Schott) by means of a thin layer of water. All relevant material properties are summarized in the Supporting Information. After thorough cleaning with UV/ozone (Jelight, UVO cleaner model 42-220), the sample surface was chemically patterned by selective deposition of 1H,1H,2H,2H-perfluorooctyltrichlorosilane (Aldrich, product number 448931). The patterns consisted of hydrophilic rectangles of typical dimension  $2.5 \times 2.5 \text{ cm}^2$  on otherwise hydrophobic surfaces. The chemical patterning was added primarily for convenience: it prevented liquid from accidentally spilling over the sample edges and facilitated the preparation of a predictable and reproducible initial condition regarding the layer thickness. While PEDOT:PSS dispersions were deposited with a Hamilton digital syringe, LEP solutions in mesitylene were spin-coated at a speed of 1500 rpm for a duration of 15 s. PEDOT:PSS dry layer thickness profiles were determined by optical absorption measurements in a transmission configuration.

Figure 2 shows three examples of IR-modulated evaporative deposition patterns using an aqueous PEDOT:PSS dispersion as well as red LEP dissolved in mesitylene. In Figure 2a,c the applied IR illumination patterns are depicted and in Figure 2b,d the corresponding deposition patterns are shown. The initial layer thicknesses were  $h_0 = 160 \mu\text{m}$  (Figure 2d) and between 1 and  $3 \mu\text{m}$  (Figure 2b). The two types of solutions exhibit a strikingly different behavior. Whereas the deposited PEDOT:PSS layer thickness is *increased*, the LEP layer thickness is *reduced* in the illuminated regions (white areas in Figure

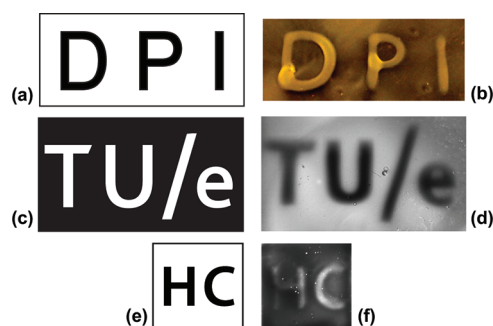


**Figure 2.** (a, c) IR illumination patterns and (b, d) corresponding modulated deposition patterns of (b) red LEP in mesitylene (image width 2 cm) and (d) PEDOT:PSS in water (image width 2.5 cm). A video of the material redistribution process corresponding to panel d is available as Supporting Information. (f) White-light emission pattern from an OLED proof-of-concept device with a thickness-modulated PEDOT:PSS hole conduction layer (image width 1.3 cm). Panel e illustrates the applied illumination pattern.

2a,c). Since the LEP concentration is enriched in the dark areas, a negative or inverted pattern is used in Figure 2a to generate a positive deposition pattern. We term the two mechanisms of operation accumulation and depletion mode, respectively.

Figure 2f shows light emission from an OLED proof-of-concept device that was processed according to the following procedures: 120 nm of indium tin oxide (ITO), metal electrodes, and bus-bar structures were deposited onto a glass substrate by sputtering and lithographic structuring. After PEDOT:PSS deposition, IR-induced pattern formation, and baking (2 min at 50 °C, followed by 6 min at 130 °C), an 80 nm thick layer of LEP was spin-coated. The electrical contacts were exposed via local laser ablation. The cathode was subsequently applied by thermal evaporation of a nominally 5 nm thick Ba layer, followed by a 100 nm thick Al layer. The device was protected against water vapor intrusion and oxidation by application of a metal lid containing a patch of calcium oxide.

### III. NUMERICAL MODEL CALCULATIONS AND COMPARISON WITH EXPERIMENTS

We developed a two-dimensional numerical model of the IR-modulated evaporative deposition process, which consists of three steps: (1) calculation of the temperature distribution due to IR illumination, (2) solvent vapor transport in the DMD enclosure and determination of the evaporative flux, and (3) simulation of the solute redistribution in the liquid layer. The material parameters that entered into the numerical calculations are listed in the Supporting Information.

**A. Temperature Distributions as a Consequence of Infrared Irradiation.** As a first step, we determine the steady-state temperature profile at the liquid–air interface of the solution layer  $T_s(x)$  taking into account laser heating, evaporative cooling as well as cooling water circulation inside the heatsink. We first consider stationary IR illumination patterns in the shape of stripes of width  $w_{\text{IR}}$ . Their length greatly exceeds the substrate thickness, such that a two-dimensional heat transfer model can be applied. The equilibration time of the temperature distribution after switching on the IR laser is on order of  $d^2/\alpha \approx 1$  s, where  $d \approx 1$  mm is the combined thickness of the solution layer, the glass substrate, and the top plate of the transparent cooling plate. The parameter  $\alpha \equiv k/(\rho c_p)$  is the thermal diffusivity,  $k$

the thermal conductivity,  $\rho$  the mass density, and  $c_p$  the specific heat capacity of the material. On the other hand, the evaporation times  $t_{\text{evap}} \equiv h_0 \rho_{\text{sol}}/j$  are typically in the range of 1–40 min, where  $h_0$  is the initial film thickness,  $\rho_{\text{sol}}$  is the solvent mass density, and  $j$  the evaporative mass flux. The thermal Péclet number  $Pe_{\text{th}} \equiv hU/\alpha < 1$ , where  $U \lesssim 100 \mu\text{m/s}$  is an estimated upper limit of the flow speed, such that thermal transport by convection inside the solution layer can be disregarded compared to conduction. Consequently, we only need to solve the steady-state heat transfer equation

$$\rho(x, y) c_p(x, y) \vec{u} \cdot \nabla T = \nabla \cdot [k(x, y) \nabla T] + \dot{q}_{\text{IR}} \quad (1)$$

where the velocity  $\vec{u} = [u_x(y), 0]$  is only nonzero in the subdomain that represents the circulating cooling water. The computational domain as well as the applicable boundary conditions (BCs) are sketched in Figure 3a. The flow profile of the cooling water is assumed to be parabolic with a maximum center speed of  $U = 10$  cm/s. The IR heating<sup>46,47</sup> is represented by the term  $\dot{q}_{\text{IR}} \equiv \alpha_{1470} I$  in eq 1, where  $\alpha_{1470}$  is the optical absorption coefficient at the laser wavelength and  $I(x, y)$  the local light intensity. Since both the numerical aperture of the imaging optics and the substrate and layer thicknesses are relatively small, we assume that  $I = I(y) \Theta_{\text{IR}}(x)$ , where  $\Theta_{\text{IR}}(x)$  is a Heaviside function that has the value 1 inside the IR illuminated region and 0 outside it. For the determination of the vertical intensity profile  $I(y)$ , we account for absorption inside the layers as well as optical reflection at the layer interfaces.

In Figure 3b we present typical profiles of the surface temperature of the solution layer for a 160  $\mu\text{m}$  thick PEDOT:PSS dispersion layer irradiated with different line widths  $w_{\text{IR}}$  that range from 0.5 to 20 mm. The center temperature  $T(0, d_{\text{liq}})$  begins to saturate for  $w_{\text{IR}} \gtrsim 5$  mm, because lateral heat conduction at  $x = 0$  becomes very small for large  $w_{\text{IR}}$ . The obliqueness of the profiles corresponding to  $w_{\text{IR}} = 15$  or 20 mm is a consequence of the finite cooling capacity of the heatsink, which begins to slightly warm up. In principle, the temperature distribution depends on the local evaporation rate due to evaporative cooling. Due to the long evaporation times  $t_{\text{evap}}$  and low evaporative fluxes, however, the influence of evaporative cooling  $Lj$  is relatively weak.

In Figure 3c we show typical profiles of the surface temperature of a 5  $\mu\text{m}$  thick LEP/mesitylene solution irradiated homogeneously over a  $w_{\text{IR}} = 25$  mm wide region except for a stripe of width  $w$  in the center. For a small values of  $w = 0.5$  mm only a small dip in the surface temperature profile is visible, whereas for  $w \gtrsim 5$  mm the temperature in the center of the nonilluminated stripe almost drops down to the cooling plate temperature  $T_{\text{cool}}$ .

The achievable spatial resolution of the temperature distribution is governed by two factors: (1) the projected size of a DMD pixel, which is approximately 25  $\mu\text{m}$  in the current setup, and (2) lateral heat conduction. The influence of the latter is determined by the combined thickness  $d$  of the liquid layer, the substrate, and the top plate of the transparent temperature control plate (typically  $d = 600$ – $1200 \mu\text{m}$  in our experiments), if their thermal conductivities are of comparable magnitude. The thermal resolution can be improved by making the substrate thinner (at the expense of the temperature modulation amplitude, which is correspondingly reduced)<sup>48</sup> or by reducing the magnification of the projection system in the setup (which increases the power density but decreases the total illuminated area).



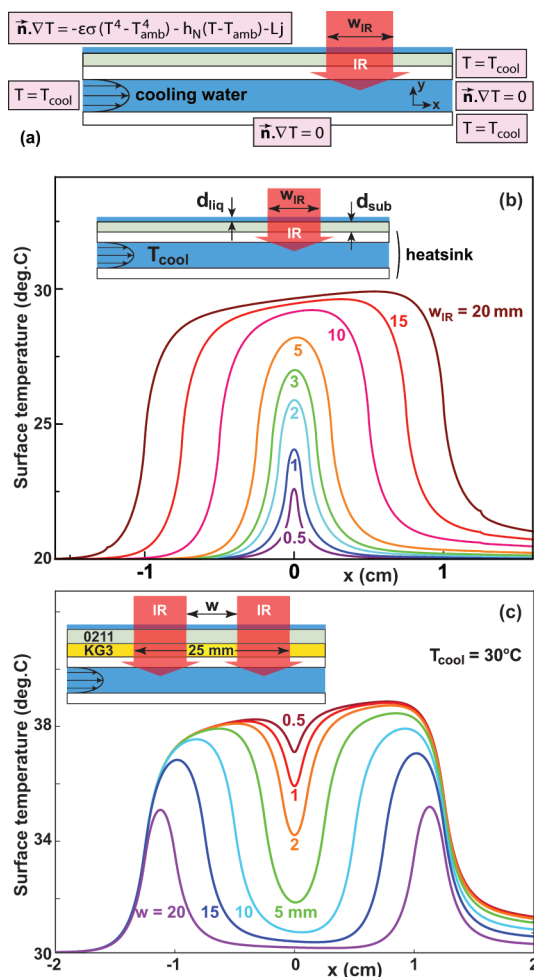


**Figure 3.** (a) Boundary conditions used for heat transfer calculations. The parameters  $\epsilon = 1$ ,  $\sigma = 5.67 \times 10^{-8} \text{ W}/(\text{m}^2 \text{ K}^4)$ ,  $h_N = 5 \text{ W}/(\text{m}^2 \text{ K})$ , and  $T_{\text{amb}} = 20^\circ\text{C}$  refer to the emissivity of the top surface, the Stefan–Boltzmann constant, the heat transfer coefficient for Newtonian cooling, and the ambient temperature, respectively. The vector  $\vec{n}$  is the outward-oriented unit normal of the computational domain. (b) Temperature profiles of the liquid–air interface  $T_s(x, y = d_{\text{liq}})$  for a 160  $\mu\text{m}$  thick PEDOT:PSS dispersion layer irradiated with different line widths  $w_{\text{IR}}$  on substrates in contact with the transparent heatsink. Soda-lime glass substrate thickness,  $d_{\text{sub}} = 1 \text{ mm}$ ; average flow speed through the heatsink, 6.7 cm/s; IR power,  $P_{100} = 2.4 \text{ W}$ . (c) Surface temperature profiles of the liquid–air interface for a 5  $\mu\text{m}$  thick LEP/mesitylene solution layer irradiated with different “negative” line widths  $w$  ranging from 0.5 to 20 mm for a constant  $w_{\text{IR}} = 25 \text{ mm}$ . The 160  $\mu\text{m}$  thick soda-lime substrate is in contact with a 1 mm thick KG3 glass plate that resides on the transparent heatsink at temperature  $T_{\text{cool}} = 30^\circ\text{C}$ .

**B. Gas-Phase Transport.** After we obtained a surface temperature profile, we model convective and diffusive solvent vapor transport in the gas phase inside the metal enclosure of the DMD system. Substantial convection is induced by air density changes  $\rho_{\text{air}} = \rho_{\text{air}}(T, s)$  as a consequence of laser heating and locally increased solvent vapor concentration  $s$ . Moreover, in some experiments, the temperature of the heatsink  $T_{\text{cool}}$  differed from ambient conditions. In order to reduce computational cost, we perform two-dimensional model calculations that correspond, in principle, to a sample and illuminated line that are infinitely long in the  $z$ -direction. Moreover, we consider only one-half of the DMD enclosure and apply

symmetry conditions at  $x = 0$ , corresponding to an illuminated line that is positioned in the center of the sample.

We solve the coupled equations for solvent vapor convection and diffusion (eq 2), heat transfer (eq 3), and momentum transport (eq 4)

$$\frac{\partial s}{\partial t} + \vec{u} \cdot \nabla s = \nabla \cdot (D_{\text{solvent}} \nabla s) \quad (2)$$

$$\rho_{\text{air}} c_{p, \text{air}} \left( \frac{\partial T}{\partial t} + \vec{u} \cdot \nabla T \right) = \nabla \cdot (k_{\text{air}} \nabla T) \quad (3)$$

$$\rho_{\text{air}} \left( \frac{\partial \vec{u}}{\partial t} + \vec{u} \cdot \nabla \vec{u} \right) = -\nabla p + \rho_{\text{air}} \vec{g} + \mu \nabla^2 \vec{u} \quad (4)$$

Here,  $s$  is the solvent vapor concentration (in units of  $\text{kg}/\text{m}^3$ ),  $D_{\text{solvent}}$  the diffusion coefficient of solvent vapor in air,  $\vec{u}$  the convection velocity of air,  $p$  the gas pressure and  $\vec{g} = (0, -g)$  the gravitational acceleration. We assume the gas phase to be incompressible in eq 4, which is permissible owing to the vanishingly small Mach numbers  $Ma \equiv u_{\text{max}}/c_s \approx 10^{-4}$  involved, where  $c_s$  is the speed of sound. We account for density changes due to thermal expansion and nonuniform solvent vapor concentrations according to eqs 3 and 5 given in the Supporting Information. We neglect the effect of temperature and composition nonuniformities on the thermal conductivity  $k$ , specific heat  $C_p$ , and viscosity  $\mu$  of air as well as on  $D_{\text{solvent}}$ .

The applicable BCs are sketched in Figure 4a. The walls of the DMD enclosure are assumed to be nonadsorbing ( $\vec{n} \cdot \nabla s = 0$ ) and maintained at ambient temperature ( $T = T_{\text{amb}}$ ). Moreover, the no-slip and no-penetration conditions hold ( $u_x = u_y = 0$ ). The left boundary  $x = 0$  is assumed to be a mirror symmetry plane. This is an approximation in view of the slight asymmetry of the temperature profiles in Figure 3 and is implemented to reduce the computational cost of the simulations. The top boundary is assumed to be at atmospheric pressure and ambient temperature and free from viscous stresses.

The BCs at the surface of the sample, the cooling plate, as well as the liquid–air interface require closer consideration. On the scale of the DMD enclosure, which is on order 20 cm, we neglect the thickness of the sample and liquid solution layer, which are on order of 1 mm, and assume that the lower boundary of the computational domain is flat. The surface temperatures of the cooling plate, the part of the sample not covered with liquid, as well as the liquid layer, as extracted from the heat transfer calculations, is applied as a Dirichlet BC for the gas-phase temperature  $T = T_{\text{IR}}(x)$ . Since the solution layers are rather thin, the viscous shear in the gas phase rather small, and the solution viscosity much larger than that of air, the surface velocities can to good approximation be assumed to vanish,  $u_x = 0 = u_y$ , not only on top of the cooling plate but also at the liquid–air interface. We assume that just above the liquid–air interface, the solvent vapor concentration corresponds to the saturation concentration<sup>55–59</sup> according to the local temperature,  $s = s_{\text{sat}}(T)$ . This implies that the evaporation rate is limited by convection and diffusion in the vapor phase. This is consistent with the long process times of 1–40 min, the process temperatures being far below the boiling point of the solvents and the absence of forced convection in the gas phase. Due to the large lateral length scales considered, we neglected the influence of the curvature of the liquid–air interface on the vapor pressure.

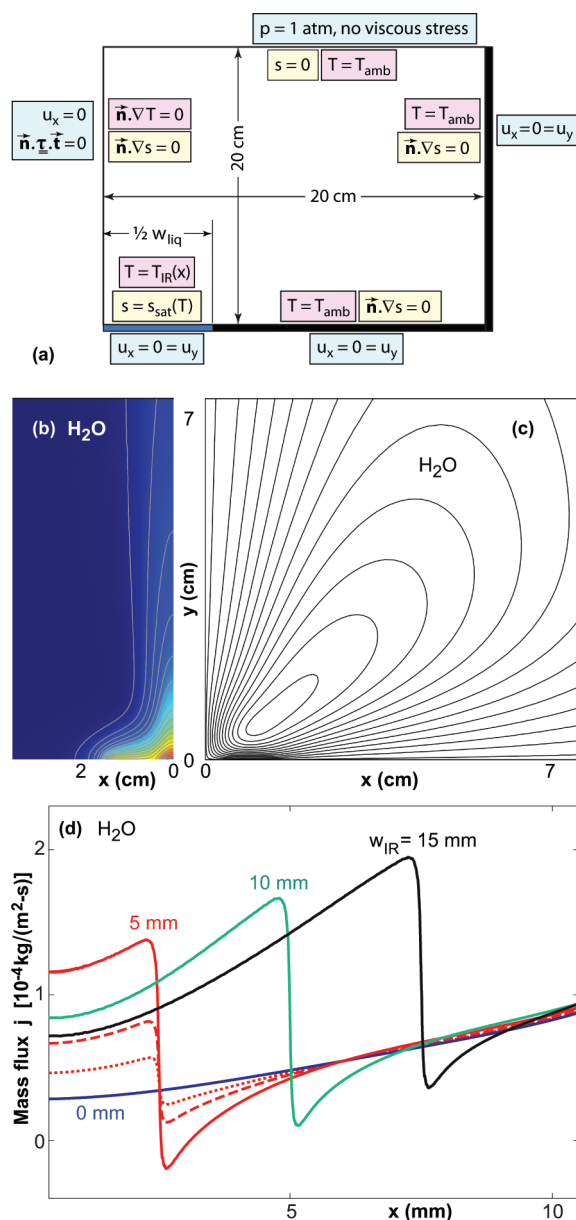


**Figure 4.** (a) Boundary conditions for solvent vapor transport in the DMD enclosure. Here,  $\vec{t}$  is a unit vector tangential to the boundary of the computational domain and  $\vec{\tau}$  is the viscous stress tensor. Isocontour plots of (b) the water vapor concentration and (c) the lateral velocity component  $u_x$  for  $w_{\text{IR}} = 5$  mm and  $P_{100} = 2.4$  W. (d) Evaporative mass flux  $j(x)$  at the liquid–air interface for different values of  $w_{\text{IR}}$  and  $P_{100}$ . The solid lines correspond to  $P_{100} = 2.4$  W and illuminated line widths of  $w_{\text{IR}} = 0$  (blue line), 5 mm (red line), 10 mm (green line), and 15 mm (black line). The dashed and dotted lines correspond to  $w_{\text{IR}} = 5$  mm and power settings of  $P_{100} = 1.2$  W and  $P_{100} = 0.6$  W, respectively.

Figure 4c depicts contour lines corresponding to constant lateral velocity  $u_x = \text{const}$  with a maximum value on order of  $u_{\text{max}} \approx 2$  cm/s for evaporation from an aqueous PEDOT:PSS layer,  $w_{\text{IR}} = 5$  mm, and  $P_{100} = 2.4$  W. The Peclet number relevant to gas-phase transport  $Pe_w = u_{\text{max}} w_{\text{liq}}/D_{\text{solvent}}$  has a numerical value around 16 for water as the solvent and approximately 6 for mesitylene, when based on typical pattern dimensions of  $w_{\text{liq}} = 2$  cm. These numerical values  $Pe_w \gg 1$  indicate that convective effects are important for the solvent vapor transport and thus determine the evaporative flux  $j(x)$ .

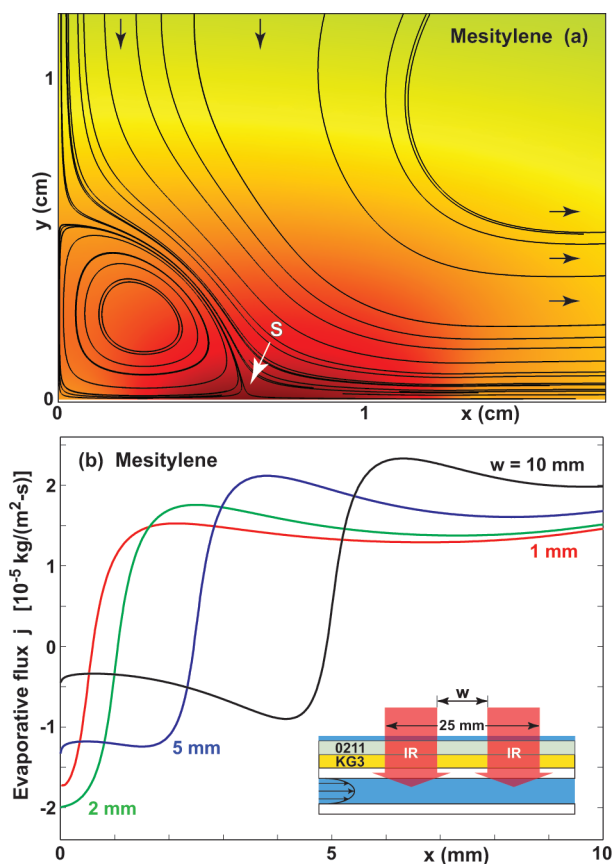
Figure 4b shows concentration contour lines that resemble the onset of a concentration boundary layer around  $x = w_{\text{liq}}/2$ , which is close to the location of the maximum of  $u_x$  visible in Figure 4c. At  $(x,y) = (0,0)$  there is a stagnation point of the convective flow pattern. A concentration plume is convected upward by the flow, which qualitatively resembles the temperature distribution above an object hotter than its environment. We note that in the case of water, the solvent evaporation adds to the convection pattern, as the density of humid air is lower than that of dry air.

Figure 4d shows typical results for the evaporative mass flux at the liquid–air interface for different values of  $w_{\text{IR}}$  and  $P_{100}$ . The solid lines correspond to  $P_{100} = 2.4$  W and illuminated line widths of  $w_{\text{IR}} = 0$  (blue line), 5 mm (red line), 10 mm (green line), and 15 mm (black line). The dashed and dotted lines correspond to  $w_{\text{IR}} = 5$  mm and power settings of  $P_{100} = 1.2$  W and  $P_{100} = 0.6$  W, respectively.

When the IR laser is off ( $w_{\text{IR}} = 0$ ), only water evaporation is driving the convection. The evaporation rate has a local minimum at the position of the stagnation point  $(x,y) = (0,0)$  and exhibits a well-studied maximum at the edge of the liquid layer  $x = w_{\text{liq}}/2 = 1.4$  cm.<sup>50–54</sup> When the IR laser is on, the mass flux at the liquid–air interface  $j(x)$  does not resemble the temperature profiles shown in Figure 3b, which exhibit a maximum near the center of the illuminated line. The shape of  $j(x)$  is influenced by two factors: (1) the stagnation point causes a reduction in  $j(x)$  toward  $x = 0$  and (2) the Dirichlet boundary condition for the concentration  $s = s_{\text{sat}}(T)$ . The latter BC induces a high lateral gradient in  $s$  close to the edge of the illuminated line, which tends to increase the evaporation rate inside the illuminated region, i.e., for  $x$  smaller but close to  $w_{\text{IR}}/2$ . It causes a decrease in its immediate vicinity at  $x \gtrsim w_{\text{IR}}/2$  and can even render  $j$  negative, which corresponds to condensation rather than evaporation, as seen in the curve corresponding to  $w_{\text{IR}} = 5$  mm and  $P_{100} = 2.4$  W. This effect is somewhat smaller for larger values of  $w_{\text{IR}}$  because the concentration boundary layer is thinner for larger values of  $x$  and thus reduces the relative importance of lateral compared to vertical concentration gradients.

In the case of water, the gas density decreases with increasing humidity, i.e., the natural convection as a consequence of solvent evaporation and local temperature increase, add up, and amplify one another. In the case of mesitylene, the molecular weight is much higher than that of air, such that the gas density increases with increasing mesitylene vapor concentration. Solvent evaporation and temperature increase thus have antagonist effects on the natural convection pattern, which is qualitatively different from the case of water. Figure 5a shows an isointensity plot of the mesitylene vapor concentration and the streamlines of the velocity distribution. In the case of water, a rising vertical plume is formed that broadens by lateral diffusion and drives a single convection roll in the enclosure. In the case of LEP/mesitylene, the combined effect of the increased density of the mesitylene vapor and the non-monotonic temperature profile induces the formation of multiple convection rolls inside the computational domain.

Figure 5a illustrates the streamlines and mesitylene vapor concentration in the vicinity of the nonilluminated line. The main flow is downward due to the higher density of mesitylene vapor compared to dry air. Besides the stagnation point at  $(0,0)$ , which is due to the mirror symmetry BC, there is a second stagnation point of the convective gas flow in Figure 5a labeled with a white arrow and the letter “S”. Its location



**Figure 5.** (a) Isointensity plot of the mesitylene vapor concentration and the streamlines for a nonilluminated line width  $w = 5$  mm and  $P_{100} = 2.4$  W and a cooling water temperature  $T_{\text{cool}} = 30$  °C. The white arrow and the label “S” indicate the location of a stagnation point, which coincides with the position of the left temperature maximum in the corresponding curve in Figure 3b. (b) Evaporative mass flux  $j(x)$  at the liquid–air interface for  $P_{100} = 2.4$  W,  $T_{\text{cool}} = 30$  °C, and different values of the nonilluminated line width  $w$ .

coincides with the position of one of the temperature maxima in the corresponding curve of Figure 3b. Figure 5b shows the evaporative mass flux  $j(x)$  at the liquid–air interface for  $P_{100} = 2.4$  W, a cooling water temperature of 30 °C, and different values of the nonilluminated line width  $w$ . The most striking feature is a substantial condensation mass flux in the central nonilluminated region, which is comparable in magnitude to the evaporative mass flux in the illuminated region.

The solvent evaporation rate  $j(x)$  with units  $\text{kg}/(\text{m}^2 \text{ s})$  is extracted from the gas-phase transport simulations by evaluating the solvent vapor flux at the liquid–air interface,  $j(x) = D_{\text{solvent}} \vec{n} \cdot \nabla s$ , and subsequently applied as a BC in the model for the solute redistribution dynamics in the liquid layer.

**C. Solute Redistribution in the Liquid Phase.** The description of the solute redistribution depends crucially on the value of the solute diffusion coefficient  $D_{\text{solute}}$  or, more precisely, on the value of the evaporative Peclet number  $Pe_{\text{evap}} \equiv h_0 j / (\rho_{\text{liq}} D_{\text{solute}})$  based on the initial layer thickness  $h_0$  and the speed of evaporation  $j / \rho_{\text{liq}}$ . Using the Stokes–Einstein relation<sup>49</sup> and a particle diameter of  $2R = 80$  nm, we estimate the initial diffusion coefficient of PEDOT:PSS particles to be  $D_{\text{solute}} = (k_B T) / (6\pi R \mu) \approx 1 \times 10^{-12} \text{ m}^2/\text{s}$ . Upon evaporation, the solute concentration and thus the solution viscosity increase, causing a further reduction of  $D_{\text{solute}}$ . This leads to the following estimate for the initial evaporative Peclet number

$Pe_{\text{evap}} \approx 24 \gg 1$ , which further increases upon solvent evaporation. For blue LEP/mesitylene, the initial film thickness is on the order  $h_0 \approx 5 \mu\text{m}$ . From dynamic light scattering experiments we estimate  $D_{\text{solute}} \approx 4 \times 10^{-11} \text{ m}^2/\text{s}$ , leading to  $Pe_{\text{evap}} \approx 0.003 \ll 1$ .

Given the large difference in  $Pe_{\text{evap}}$ , we developed separate models for the two material systems that are described in the following subsections. Potential short-comings of the model calculations are discussed in the Supporting Information.

**1. Thin Films—LEP in Mesitylene.** For small  $Pe_{\text{evap}}$ , the solute concentration is to a good approximation uniform in the  $y$ -direction. As a consequence, we can consider the one-dimensional convection–diffusion equation<sup>63–67</sup> for a non-volatile solute that adsorbs neither at the liquid–solid nor the liquid–air interface

$$h \frac{\partial \langle c \rangle}{\partial t} + \left( \frac{h^2}{2\mu} \frac{\partial \gamma}{\partial x} - \frac{h^3}{3\mu} \frac{\partial p}{\partial x} \right) \frac{\partial \langle c \rangle}{\partial x} = \frac{\partial}{\partial x} \left( h D_{\text{solute}} \frac{\partial \langle c \rangle}{\partial x} \right) + \frac{j}{\rho_{\text{liq}}} \langle c \rangle \quad (5)$$

which is coupled with the lubrication equation describing the fluid redistribution<sup>68</sup>

$$\frac{\partial h}{\partial t} + \frac{\partial}{\partial x} \left( \frac{h^2}{2\mu} \frac{\partial \gamma}{\partial x} - \frac{h^3}{3\mu} \frac{\partial p}{\partial x} \right) = - \frac{j}{\rho_{\text{liq}}} \quad (6)$$

Here, we introduced the height-averaged concentration distribution  $\langle c \rangle \equiv 1/h \int_0^h c(x,y) dy$ , as well as the augmented pressure in the thin liquid film

$$p = \rho_{\text{liq}} g h - \gamma \frac{\partial^2 h}{\partial x^2} \quad (7)$$

where  $\rho_{\text{liq}}$  is the mass density of the solution and  $g = 9.81 \text{ m/s}^2$  the gravitational acceleration. The terms on the right of eq 7 correspond to the contributions of hydrostatic and capillary pressure, respectively. We chose the size of the computational domain  $L = 12$  mm to be large enough such that it did not affect the resulting distribution in the vicinity of the nonilluminated line. We used the following BCs to solve eqs 5 and 6

$$\frac{\partial \langle c \rangle}{\partial x}(x=0) = 0 = \frac{\partial \langle c \rangle}{\partial x}(x=L) \quad (8)$$

$$\frac{\partial h}{\partial x}(x=0) = 0 = \frac{\partial h}{\partial x}(x=L) \quad (9)$$

$$\frac{\partial p}{\partial x}(x=0) = 0 = \frac{\partial p}{\partial x}(x=L) \quad (10)$$

which correspond to mirror-symmetry at both ends of the computational domain at  $x = 0$  and  $x = L$ .

Figure 6a shows the resulting nondimensional solute distribution represented by  $h \langle c \rangle / (h_0 c_0)$ , which is proportional to the total solute mass per unit area  $\int_0^h c(x,y) dy$ . Here,  $h_0$  and  $c_0$  are the initial film thickness and LEP concentration, respectively. The simulations have been terminated at the instant  $t = t_{\text{th}}$  when the minimum film thickness at any location falls below a threshold value close to zero, i.e., when the film locally dries. At this instant, the evaporative flux  $j(x)$ , which is determined from the steady-state gas-phase transport simulations using the BC  $c = c_{\text{sat}}(T)$  at the entire base area of the



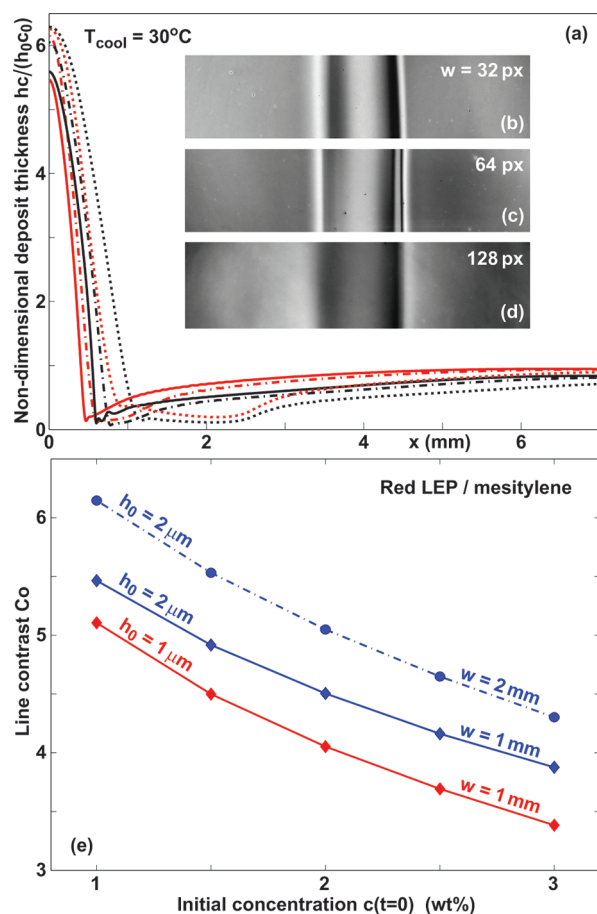


**Figure 6.** (a) Nondimensional deposit thickness  $h(c)/(h_0c_0)$  for three values of  $w = 1$  mm (solid lines), 2 mm (dash-dotted lines), and 5 mm (dotted lines) and two values of  $h_0 = 2$  (red lines) and  $4 \mu\text{m}$  (black lines). (b–d) Microscope images of a pattern induced in a solution of red LEP in mesitylene for different nonilluminated line widths of (b)  $w = 32$  pixels, (c) 64 pixels, and (d) 128 pixels corresponding to  $w = 0.88$ , 1.7, and 3.4 mm, respectively. The grayscale contrast arises from optical interference. The substrate temperature was  $T_{\text{cool}} = 30^\circ\text{C}$ . The illumination spectrum was centered around  $\lambda = 450$  nm with a spectral bandwidth of  $\Delta\lambda = 25$  nm. (e) Simulation results for the achievable line contrast as a function of the initial concentration  $c_0$  for initial film thicknesses of  $h_0 = 1$  and  $2 \mu\text{m}$  and two values of  $w = 1$  mm (diamonds) and 2 mm (circles).

initially deposited solution layer, ceases to be a good approximation. For  $t > t_{\text{th}}$ , the flux  $j$  would become intrinsically time-dependent, as new contact lines are formed at the edges of the growing, already dried regions. Although there is still solvent present in some regions at  $t = t_{\text{th}}$ , the solute distribution has effectively converged to its final state, because the increased solution viscosity effectively prevents further redistribution.

The sets of lines in Figure 6a correspond to initial film thicknesses of  $h_0 = 2$  and  $4 \mu\text{m}$ , respectively, as well as nonilluminated line widths  $w$  of 1 mm (solid lines), 2 mm (dash-dotted lines), and 5 mm (dotted lines). Two striking features are that both the peak values and the full width at half-maximum values of the curves are relatively independent of  $w$ , which changes by a factor of 5. Figures 6b–d show experimental microscope images for nonilluminated line widths of 32, 64, and 128 pixels, which correspond to 0.88, 1.7, and 3.4 mm. As in the simulations, the material accumulated in the

nonilluminated region and the line width varies only slightly with  $w$ .

We define the line contrast,  $Co$ , as the ratio of the deposit thickness in the center of a line and far away from it,  $h(x=0)/h(x=L)/h_0c_0$ , from which we deduce  $Co \approx 6$  for the simulation results in Figure 6a. From the few interference fringes visible in the experimental images of Figure 6b–d, we conclude that the contrast in the experimental images is significantly smaller. Very likely the contrast is overestimated in the simulations, which were based on the nominal initial concentration of  $c_0 = 1$  wt %, because the concentration increased during the spin-coating process and due to the time delay caused by removal of the sample from the spin-coater, transfer to the DMD lab, and its placement in the DMD enclosure before the start of the IR illumination. In Figure 6e we plotted  $Co$  as a function of initial concentration, which exhibits a systematic decrease with increasing  $c_0$ .

**2. Thick Films—PEDOT:PSS.** For large  $Pe_{\text{evap}}$ , we need to solve the full two-dimensional convection–diffusion equation coupled with the Navier–Stokes equation

$$\frac{\partial c}{\partial t} + \vec{u} \cdot \nabla c = \nabla \cdot (D_{\text{solute}} \nabla c) \quad (11)$$

$$\rho_{\text{liq}} \left( \frac{\partial \vec{u}}{\partial t} + \vec{u} \cdot \nabla \vec{u} \right) = -\nabla p + \rho_{\text{liq}} \vec{g} + \mu \nabla^2 \vec{u} \quad (12)$$

where the density  $\rho_{\text{liq}}$  is assumed to be constant, whereas the viscosity  $\mu$  and solute diffusion coefficient  $D_{\text{solute}}$  are concentration-dependent.

Equations 11 and 12 are solved with an arbitrary Lagrangian–Eulerian (ALE) scheme in order to capture the deformation of the liquid–air interface. We chose the domain width  $L = 8$  mm large enough such that the deposit distribution near the illuminated line was insensitive to the numerical value of  $L$ . The applicable BCs are

$$u_x(y=0) = u_y(y=0) = 0, \quad \frac{\partial c}{\partial y}(y=0) = 0 \quad (13)$$

$$u_x = 0, \quad \frac{\partial u_y}{\partial x} = 0, \quad \frac{\partial c}{\partial x} = 0 \quad \text{at } x = 0 \text{ and } L \quad (14)$$

$$\vec{n} \cdot \nabla c = \frac{cj}{\rho_{\text{liq}} D_{\text{solute}}} \quad \vec{n} \cdot (\vec{u} - \vec{u}_{\text{int}}) = -\frac{j}{\rho_{\text{liq}}} \quad (15)$$

$$\vec{n} \cdot \vec{\tau} \cdot \vec{t} = \vec{t} \cdot \nabla_s \gamma \quad p - \vec{n} \cdot \vec{\tau} \cdot \vec{n} = \gamma \nabla_s \cdot \vec{n} \quad (16)$$

where  $\vec{n}$  and  $\vec{t}$  are the unit normal and tangential vectors of the liquid–air interface,  $\vec{\tau}$  is the viscous stress tensor,  $\vec{u}_{\text{int}}$  is the displacement speed of the liquid–air interface, and  $\nabla_s$  is the surface gradient operator.<sup>61</sup>

Equations 13 represent no-slip, no-penetration, and no-adsorption at the solid–liquid interface. Equations 14 correspond to mirror-symmetry at the left and right domain boundaries. Equations 15 describe the evaporative mass loss at the liquid–air interface and the corresponding concentration increase of the solute, which is assumed to be nonadsorbing and nonvolatile.<sup>60</sup> Equations 16 express the tangential and normal stress discontinuities at a liquid–air interface, where the stresses in the gas phase were neglected owing to the low density and viscosity of air and the absence of forced convection.<sup>61</sup> The BCs are summarized in Figure 7a. The



initial conditions were a uniform solute distribution  $\langle c \rangle = c_0 = 1$  wt % and a uniform height profile  $h = h_0 = 150 \mu\text{m}$ .

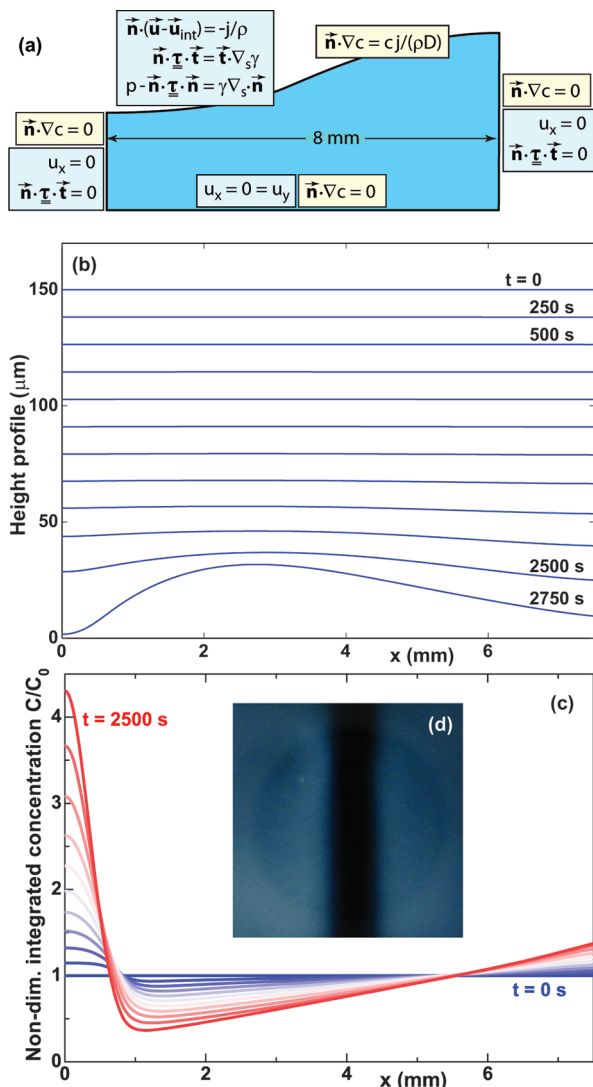


**Figure 7.** (a) Boundary conditions used for the two-dimensional ALE simulations. (b,c) Time evolution of the (b) height profile and (c) vertically integrated concentration profile for  $h_0 = 150 \mu\text{m}$ ,  $P_{100} = 2.4$  W, and  $w_{\text{IR}} = 64$  pixel. (d) Experimental PEDOT:PSS line pattern corresponding to parameter values  $h_0 = 250 \mu\text{m}$ ,  $P_{100} = 2.4$  W, and  $w_{\text{IR}} = 64$  pixels. Image width approximately 12 mm.

A crucial aspect for dispersions of PEDOT:PSS nanoparticles or other solutes of effectively high molecular weight is the formation of a solute-rich skin layer<sup>62</sup> at the liquid–air interface induced by the exceedingly small solute diffusion coefficient. This skin effect self-enhances due to the concentration dependence of  $\mu$  and  $D_{\text{solute}}$  and effectively suppresses thermo- and solutocapillary shear flows inside the solution layer. This can be understood by considering the shear stress discontinuity in eqs 16. Since the viscous stresses in the gas phase can be neglected relative to the viscous stresses in the liquid, the remaining dominant terms in the case of a horizontal liquid–air interface are

$$\frac{\partial u_x}{\partial y} = \frac{1}{\mu(c)} \frac{\partial \gamma}{\partial x} \quad \text{at } y = h \quad (17)$$

Consequently, shear flows induced by surface tension gradients are diminished severely, if the bulk viscosity at the liquid–air interface increases as a consequence of skin formation, whereas pressure-driven bulk flow is much less affected.

Unfortunately, the numerical implementation cannot handle diffusion coefficients smaller than approximately  $10^{-10} \text{ m}^2/\text{s}$ , due to stability problems when concentration gradients exceed a certain limit. Therefore, we could not model the dynamics of the skin-formation process directly, and resorted to assuming a diffusion coefficient of approximately  $10^{-10} \text{ m}^2/\text{s}$  and neglecting the influence of thermo- and solutocapillary shear stresses. This hardly affects the lateral solute distribution, since sideways diffusive solute transport was relatively insignificant at the lateral length scales  $w_{\text{IR}} \gtrsim 1 \text{ mm}$  we considered.

Figure 7b,c illustrates the time evolution of the height profile  $h(x,t)$  and vertically integrated concentration profiles  $C(x,t) \equiv \int_0^h c(x,y,t) dy$ , respectively. The latter quantity is proportional to the final dry layer thickness, after all the solvent has evaporated.

For most of the evaporation process, the PEDOT:PSS dispersion thickness remained effectively uniform owing to the influence of capillary and hydrostatic pressure and the relatively large initial film thickness. Due to the enhanced evaporation rate in the illuminated regions, lateral material transport is induced toward the heated regions, which causes the accumulation observed in Figures 2d and 7c,d.

We have studied the influence of the relevant operating parameters on the solute deposition process experimentally. Figure 8a compares PEDOT:PSS dry layer thickness profiles after IR illumination of a  $w_{\text{IR}} = 64$  pixel (1.6 mm) wide line for different initial film thicknesses. In Figure 8b we present PEDOT:PSS dry layer thickness profiles  $h_{\text{dry}}(x)$  after IR illumination in the shape of a  $w_{\text{IR}} = 64$  pixel (1.6 mm) wide line for different laser powers  $P_{100}$ . Figure 8c shows the contrast of the dry material distribution, which is defined as the ratio of the maximum and minimum film thickness values. Open symbols correspond to edge-supported samples, whereas solid symbols to samples on the transparent heatsink.

The contrast increases approximately linearly with  $P_{100}$ , which we interpret to be a consequence of more and more liquid being evaporated in the illuminated region relative to evaporation from unilluminated zones. The solid line in Figure 8c corresponds to the results of our numerical model for a heatsink temperature of  $20^\circ\text{C}$ , which is in excellent, quantitative agreement with the experimental results.

#### IV. CONCLUSIONS

We have developed a highly flexible and adaptable system for modulated evaporative material deposition from liquid solutions. Two operating modes have been identified that depend primarily on the film thickness and the molecular weight of the solute. Solutes of high molecular weight that form a skin at the liquid–air interface of “thick” films tend to accumulate in the irradiated regions, where the evaporation rate is highest. Contrary to that, the redistributions of low molecular weight solutes in “thin” films is primarily in response to thermo- and solutocapillary surface tension gradients, which can result in a depletion of material in the illuminated regions.

We presented experimental results for aqueous PEDOT:PSS dispersions as well as solutions of light-emitting polymers in an organic solvent. We developed numerical models for the deposition process comprising (1) the heat transfer as a consequence of infrared irradiation, (2) solvent evaporation and associated vapor transport in the gas phase, as well as (3)

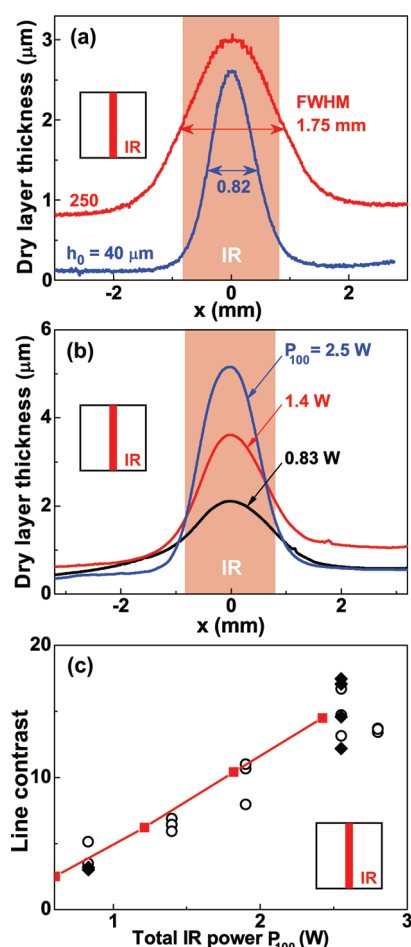


**Figure 8.** (a) Transverse PEDOT:PSS dry layer thickness  $h_{\text{dry}}(x)$  for line illumination ( $w_{\text{IR}} = 64$  pixels, as indicated by the red rectangle) and two different values of  $h_0$ . (b) Transverse PEDOT:PSS dry layer thickness profile  $h_{\text{dry}}(x)$  for an illuminated line width of  $w_{\text{IR}} = 64$  pixels (as indicated by the red rectangle) and different IR powers. Initial film thickness  $h_0 = 160 \mu\text{m}$ . (c) Contrast of the PEDOT:PSS material distribution for  $w_{\text{IR}} = 64$  pixels and  $h_0 = 160 \mu\text{m}$  as a function of IR power. Open symbols correspond to edge-supported samples, solid symbols to samples processed on the heatsink, and the line to numerical simulations.

solute redistribution inside the liquid layer. Excellent agreement between experimental and numerical results has been achieved, which provides a sound basis for future optimization of the system configuration and illumination strategies.

## ■ ASSOCIATED CONTENT

### Supporting Information

A live video of the material redistribution process of a PEDOT:PSS dispersion layer, the material properties used in the simulations, as well as a list of potential shortcomings of the numerical model. This material is available free of charge via the Internet at <http://pubs.acs.org>.

## ■ AUTHOR INFORMATION

### Corresponding Author

\*E-mail: [a.a.darhuber@tue.nl](mailto:a.a.darhuber@tue.nl).

### Notes

The authors declare no competing financial interest.

## ■ ACKNOWLEDGMENTS

This research forms part of the research programme of the Dutch Polymer Institute (DPI), project #640. The authors wish to thank Charlotte Kjellander, Maosheng Ren, Ike de Vries, and their colleagues at Holst Centre/TNO (Eindhoven) for the inspiring collaboration. Moreover, they are grateful to Leo van Hout for his assistance with designing the transparent temperature control plate. Jürgen Sweelssen is acknowledged for measuring viscosity and surface tension data for PEDOT:PSS and LEP solutions. The authors are grateful to Dorothee Hermes and Peter Rensing of Holst Centre/TNO (Eindhoven) for their help with the OLED processing.

## ■ REFERENCES

- (1) Hebner, T. R.; Wu, C. C.; Marcy, D.; Lu, M. H.; Sturm, J. C. *Appl. Phys. Lett.* **1998**, *72*, 519–521.
- (2) Bharathan, J.; Yang, Y. *Appl. Phys. Lett.* **1998**, *72*, 2660–2662.
- (3) Björnholm, T.; Hassenkam, T.; Reitzel, N. *J. Mater. Chem.* **1999**, *9*, 1975–1990.
- (4) Sirringhaus, H.; Kawase, T.; Friend, R. H.; Shimoda, T.; Inbasekaran, M.; Wu, W.; Woo, E. P. *Science* **2000**, *290*, 2123–2126.
- (5) Calvert, P. *Chem. Mater.* **2001**, *13*, 3299–3305.
- (6) Tracz, A.; Jeszka, J. K.; Watson, M. D.; Pisula, W.; Müllen, K.; Pakula, T. *J. Am. Chem. Soc.* **2003**, *125*, 1682–1683.
- (7) Mitzi, D. B. *J. Mater. Chem.* **2004**, *14*, 2355–2365.
- (8) Chang, P. C.; Lee, J.; Huang, D.; Subramanian, V.; Murphy, A. R.; Fréchet, J. M. J. *Chem. Mater.* **2004**, *16*, 4783–4789.
- (9) Kawase, T.; Moriya, S.; Newsome, C. J.; Shimoda, T. *Jpn. J. Appl. Phys.* **2005**, *44*, 3649–3658.
- (10) Shimoda, T.; Matsuki, Y.; Furusawa, M.; Aoki, T.; Yudasaka, I.; Tanaka, H.; Iwasawa, H.; Wang, D.; Miyasaka, M.; Takeuchi, Y. *Nature* **2006**, *440*, 783–786.
- (11) Park, J.-U.; Hardy, M.; Kang, S. J.; Barton, K.; Adair, K.; Mukhopadhyay, D. K.; Lee, C. Y.; Strano, M. S.; Alleyne, A. G.; Georgiadis, J. G.; et al. *Nature Mater.* **2007**, *6*, 782–789.
- (12) Vak, D.; Kim, S.-S.; Jo, J.; Oh, S.-H.; Na, S.-I.; Kim, J.; Kim, D.-Y. *Appl. Phys. Lett.* **2007**, *91*, 081102.
- (13) Ohe, T.; Kuribayashi, M.; Yasuda, R.; Tsuboi, A.; Nomoto, K.; Satori, K.; Itabashi, M.; Kasahara, J. *Appl. Phys. Lett.* **2008**, *93*, 053303.
- (14) Sekitani, T.; Noguchi, Y.; Zschieschang, U.; Klauk, H.; Someya, T. *Proc. Natl. Acad. Sci. U. S. A.* **2008**, *105*, 4976–4980.
- (15) Karakawa, M.; Chikamatsu, M.; Yoshida, Y.; Oishi, M.; Azumi, R.; Yase, K. *Appl. Phys. Exp.* **2008**, *1*, 061802.
- (16) Lucas, L. A.; DeLongchamp, D. M.; Richter, L. J.; Kline, R. J.; Fischer, D. A.; Kaafarani, B. R.; Jabbour, G. E. *Chem. Mater.* **2008**, *20*, 5743–5749.
- (17) Keivanidis, P. E.; Khong, S.-H.; Ho, P. K. H.; Greenham, N. C.; Friend, R. H. *Appl. Phys. Lett.* **2009**, *94*, 173303.
- (18) Liu, S.; Wang, W. M.; Briseno, A. L.; Mannsfeld, S. C. B.; Bao, Z. *Adv. Mater.* **2009**, *21*, 1217–1232.
- (19) Treossi, E.; Liscio, A.; Feng, X.; Palermo, V.; Müllen, K.; Samori, P. *Appl. Phys. A: Mater. Sci. Process.* **2009**, *95*, 15–20.
- (20) Giroto, C.; Rand, B. P.; Genoe, J.; Heremans, P. *Sol. Energ. Mater. Sol. C* **2009**, *93*, 454–458.
- (21) Lim, J. A.; Lee, H. S.; Lee, W. H.; Cho, K. *Adv. Funct. Mater.* **2009**, *19*, 1515–1525.
- (22) Lim, J. A.; Lee, W. H.; Kwak, D.; Cho, K. *Langmuir* **2009**, *25*, 5404–5410.
- (23) Sele, C. W.; Kjellander, B. K. C.; Niesen, B.; Thornton, M. J.; Van der Putten, J. B. P. H.; Myny, K.; Wondergem, H. J.; Moser, A.; Resel, R.; Van Breemen, A. J. J. M.; et al. *Adv. Mater.* **2009**, *21*, 4926–4931.
- (24) Derby, B. *Annu. Rev. Mater. Res.* **2010**, *40*, 395–414.
- (25) Hwang, J. K.; Cho, S.; Dang, J. M.; Kwak, E. B.; Song, K.; Moon, J.; Sung, M. M. *Nature Nanotechnol.* **2010**, *5*, 742–748.
- (26) Abdellah, A.; Fabel, B.; Lugli, P.; Scarpa, G. *Org. Electron.* **2010**, *11*, 1031–1038.

- (27) Guo, Y.; Di, C.; Liu, H.; Zheng, J.; Zhang, L.; Yu, G.; Liu, Y. *ACS Nano* **2010**, *4*, 5749–5754.
- (28) Tellier, J.; Malic, B.; Kuscser, D.; Trefalt, G.; Kosec, M. *J. Am. Ceram. Soc.* **2011**, *94*, 2834–2840.
- (29) De Luca, G.; Pisula, W.; Credgington, D.; Treossi, E.; Fenwick, O.; Lazzerini, G. M.; Dabirian, R.; Orgiu, E.; Liscio, A.; Palermo, V.; et al. *Adv. Funct. Mater.* **2011**, *21*, 1279–1295.
- (30) Rogowski, R. Z.; Dzwilewski, A.; Kemerink, M.; Darhuber, A. A. *J. Phys. Chem. C* **2011**, *115*, 11758–11762.
- (31) Nakashima, H.; Higgins, M. J.; O'Connell, C.; Torimitsu, K.; Wallace, G. G. *Langmuir* **2012**, *28*, 804–811.
- (32) Hofkens, J.; Hotta, J.; Sasaki, K.; Masuhara, H.; Iwai, K. *Langmuir* **1997**, *13*, 414–419.
- (33) Sigel, R.; Fytas, G.; Vainos, N.; Pispas, S.; Hadjichristidis, N. *Science* **2002**, *297*, 67–69.
- (34) Dietzel, M.; Poulidakos, D. *Phys. Fluids* **2005**, *17*, 102106.
- (35) Kossyrev, P. A.; Bockstaller, M. R.; Thomas, E. L. *Langmuir* **2005**, *21*, 814–817.
- (36) Nabetani, Y.; Yoshikawa, H.; Grimsdale, A. C.; Müllen, K.; Masuhara, H. *Langmuir* **2007**, *23*, 6725–6729.
- (37) Louchev, O. A.; Juodkazis, S.; Murazawa, N.; Wada, S.; Misawa, H. *Opt. Express* **2008**, *16*, 5673–5680.
- (38) Anyfantakis, M.; Loppinet, B.; Fytas, G.; Pispas, S. *Opt. Lett.* **2008**, *33*, 2839–2841.
- (39) Delville, J.-P.; Hugonnot, E.; Labrugere, C.; Cohen-Bouhacina, T.; Delville, M.-H. *J. Phys. Chem. C* **2010**, *114*, 19782–19791.
- (40) Heintz, E. *J. Phys. Radium* **1946**, *7*, 336–341.
- (41) Cormier, M.; Blanchard, M.; Rioux, M.; Beaulieu, R. *Appl. Opt.* **1978**, *17*, 3622–3626.
- (42) Loulergue, J.-C.; Levy, Y.; Imbert, C. *Opt. Commun.* **1983**, *45*, 149–154.
- (43) Hitt, D. L.; Smith, M. K. *Phys. Fluids A* **1993**, *5*, 2624–2632.
- (44) Grigoriev, R. O. *Phys. Fluids* **2002**, *14*, 1895–1909.
- (45) Garnier, N.; Grigoriev, R. O.; Schatz, M. *Phys. Rev. Lett.* **2003**, *91*, 5–8.
- (46) Eichler, H. J. *Laser-Induced Dynamic Gratings*; Springer: Berlin, 1986.
- (47) Cordero, M. L.; Verneuil, E.; Gallaire, F.; Baroud, C. N. *Phys. Rev. E* **2009**, *79*, 011201.
- (48) Darhuber, A. A.; Troian, S. M.; Wagner, S. J. *Appl. Phys.* **2002**, *91*, 5686–5693.
- (49) Beenakker, C. W. J. *Physica A* **1984**, *128*, 48–81.
- (50) Potash, M., Jr.; Wayner, P. C., Jr. *Int. J. Heat Mass Transfer* **1972**, *15*, 1851–1863.
- (51) Moosman, S.; Homsy, G. M. *J. Colloid Interface Sci.* **1980**, *73*, 212–223.
- (52) Deegan, R. D.; Bakajin, O.; Dupont, T. F.; Huber, G.; Nagel, S.; Witten, T. A. *Nature* **1997**, *389*, 827–829.
- (53) Cachile, M.; Bénichou, O.; Poulard, C.; Cazabat, A. M. *Langmuir* **2002**, *18*, 8070–8078.
- (54) Eggers, J.; Pismen, L. M. *Phys. Fluids* **2010**, *22*, 112101.
- (55) Hu, H.; Larson, R. G. *J. Phys. Chem. B* **2002**, *106*, 1334–1344.
- (56) Sultan, E.; Boudaoud, A.; Ben Amar, M. *J. Eng. Math.* **2004**, *50*, 209–222.
- (57) Mollaret, R.; Sefiane, K.; Christy, J. R. E.; Veyret, D. *Chem. Eng. Res. Des.* **2004**, *82*, 471–480.
- (58) Bhardwaj, R.; Fang, X.; Attinger, D. *New J. Phys.* **2009**, *11*, 075020.
- (59) Semenov, S.; Starov, V. M.; Rubio, R. G.; Velarde, M. G. *Coll. Surf. A: Physicochem. Eng. Aspects* **2010**, *372*, 127–134.
- (60) Slattery, J. C.; Sagis, L.; Oh, E.-S. *Interfacial Transport Phenomena*; Springer: New York, 2007.
- (61) Deen, W. M. *Advanced Transport Phenomena*; Oxford University Press: New York, 1998.
- (62) Okuzono, T.; Ozawa, K.; Doi, M. *Phys. Rev. Lett.* **2006**, *97*, 136103.
- (63) Jensen, O. E.; Grotberg, J. B. *Phys. Fluids A* **1993**, *5*, 58–68.
- (64) Wilson, S. K. *IMA J. Appl. Math.* **1993**, *50*, 149–166.
- (65) Weidner, D. E.; Schwartz, L. W.; Eley, R. R. *J. Colloid Interface Sci.* **1996**, *179*, 66–75.
- (66) Eres, M. H.; Weidner, D. E.; Schwartz, L. W. *Langmuir* **1999**, *15*, 1859–1871.
- (67) Gaskell, P. H.; Jimack, P. K.; Sellier, M.; Thompson, H. M. *Phys. Fluids* **2006**, *18*, 013601.
- (68) Oron, A.; Davis, S. H.; Bankoff, S. G. *Rev. Mod. Phys.* **1997**, *69*, 931–980.